Syngap1 regulates experience-dependent cortical ensemble plasticity by promoting in vivo excitatory synapse strengthening

Nerea Llamosas[a], Sheldon D. Michaelson[a], Thomas Vaissiere[a], Camilo Rojas[a], Courtney A. Miller[a,b], and Gavin Rumbaugh[a,b,1]

[a]Department of Neuroscience, The Scripps Research Institute, Jupiter, FL 33458; and [b]Department of Molecular Medicine, The Scripps Research Institute, Jupiter, FL 33458

Edited by Hugo Bellen, Baylor College of Medicine, Houston, TX, and approved July 7, 2021 (received for review January 22, 2021)

A significant proportion of autism risk genes regulate synapse function, including plasticity, which is believed to contribute to behavioral abnormalities. However, it remains unclear how impaired synapse plasticity contributes to network-level processes linked to adaptive behaviors, such as experience-dependent ensemble plasticity. We found that *Syngap1*, a major autism risk gene, promoted measures of experience-dependent excitatory synapse strengthening in the mouse cortex, including spike-timing–dependent glutamatergic synaptic potentiation and presynaptic bouton formation. Synaptic depression and bouton elimination were normal in *Syngap1* mice. Within cortical networks, *Syngap1* promoted experience-dependent increases in somatic neural activity in weakly active neurons. In contrast, plastic changes to highly active neurons from the same ensemble that paradoxically weaken with experience were unaffected. Thus, experience-dependent excitatory synapse strengthening mediated by *Syngap1* shapes neuron-specific plasticity within cortical ensembles. We propose that other genes regulate neuron-specific weakening within ensembles, and together, these processes function to redistribute activity within cortical networks during experience.

autism | sensory | *Syngap1* | plasticity | cortex

Autism risk genes converge on several neurobiological functions, including the regulation of synapse biology (1–3). Synapse processes directly controlled by autism spectrum disorder (ASD) risk genes include de novo synapse formation, synapse maturation, and activity-driven changes in synapse function (i.e., synapse plasticity). Synapse plasticity, especially in cortical excitatory neurons, is a process enabling neural circuits to store new information, which is essential for experience-dependent modifications of behavior to promote survival (4, 5). Thus, risk genes are thought to contribute to ASD etiology by disrupting how neural circuits change in response to novel experiences, which in turn contributes to maladaptive behaviors. However, the study of risk gene biology and their relationship to neural plasticity is largely restricted to reduced biological preparations that focus on isolated changes to a small subset of synapses. Therefore, it is unclear how risk gene–driven regulation of synapse plasticity contributes to changes in neural dynamics within intact functional networks known to drive adaptive behaviors.

Neuronal ensembles, or groups of coactivated neurons, are thought to be the direct neural substrate of cognitive processes and behavior (6). In cortex, ensemble plasticity is a multidimensional process that reflects the distribution of distinct cellular plasticity mechanisms across individual neuronal components within the assembly. For example, neurons within the same sensory-evoked cortical ensemble can undergo either increases or decreases in activity in response to the same sensory experience (7–9). While this general phenomenon has been observed in multiple contexts, it is unclear how neurons within the same functional network can have opposing changes to enduring neuronal activity in response to the same sensory experience. One way that this may occur is through the simultaneous activation of distinct forms of experience-dependent plasticity that are differentially distributed throughout neurons that comprise a functional network. Indeed, sensory experience drives the induction of Hebbian-type synaptic plasticity that can strengthen or weaken excitatory synaptic input onto sensory-responsive neurons (10). Experience-dependent circuit plasticity is not limited to changes in excitatory synaptic strength. Robust changes to the function and connectivity of GABAergic interneurons within cortical microcircuits also occurs in response to novel experience, which in turn regulates the output of pyramidal neurons (11–13). Moreover, intrinsic changes to neuronal excitability have also been observed, and in combination with changes to GABAergic function, these collective processes are thought to maintain a set firing rate within networks even as activity is redistributed among individual neurons (8, 14, 15).

We propose that experience induces heterogenous changes in activity within neurons of a cortical assembly through cellular processes controlled, at least in part, by genetic mechanisms linked to ASD risk. This hypothesis originates from the clear overrepresentation of ASD risk genes that regulate the neurobiology of synapses and synapse plasticity (1–3). However, because of the multidimensional nature of cortical network plasticity, one cannot infer how a gene influences experience-dependent changes in distributed network dynamics when the function of the gene has only been studied in isolated subcellular structures, such as synapses. It is

Significance

Many autism risk genes, such as *Syngap1*, regulate synapse plasticity, and disruptions to this subcellular process are thought to underlie behavioral deficits. However, behavior emerges through experience-driven dynamics within neural ensembles or groups of coactivated neurons. It is currently unclear how genetic regulation of synapse plasticity contributes to experience-dependent changes to cortical ensemble activity. Our data demonstrate that disruptions to synapse-level strengthening mechanisms in *Syngap1* mice underlies impairments to balanced plasticity within cortical ensembles driven by novel sensory experience. Because not all neurons in ensembles were sensitive to *Syngap1* regulation, we propose that additional genetic mechanisms are also initiated in response to experience to effectively redistribute activity within cortical networks.

Author contributions: N.L., C.A.M., and G.R. designed research; N.L. performed research; S.D.M. and T.V. contributed new reagents/analytic tools; N.L., S.D.M., T.V., C.R., and G.R. analyzed data; and N.L. and G.R. wrote the paper.

The authors declare no competing interest.

This article is a PNAS Direct Submission.

[1]To whom correspondence may be addressed. Email: grumbaug@scripps.edu.

This article contains supporting information online at https://www.pnas.org/lookup/suppl/doi:10.1073/pnas.2100579118/-/DCSupplemental.

Published August 17, 2021.

therefore important to study major ASD risk genes in the context of intact functional networks. Doing so will help to elucidate how their influence over molecular and cellular functions contribute to intermediate network-level processes more directly linked to behaviors, such as cortical ensemble plasticity.

In this study, we investigated how a major ASD risk gene, *SYNGAP1*/*Syngap1* (HUMAN/mouse–mouse only from now on), regulates specific aspects of cellular plasticity in vivo and how this process shapes experience-dependent ensemble plasticity with sensory-responsive cortical networks. The *Syngap1* gene, which is a major autism risk factor (16), is a robust regulator of various forms of long-term potentiation (LTP) (17), a cellular model of Hebbian plasticity. It regulates LTP through control of excitatory synapse structure and function by gating NMDA receptor-dependent regulation of AMPA receptor trafficking and dendritic spine size (18–20). The role of *Syngap1* in regulating synapse plasticity has been observed by various researchers across distinct neuronal subtypes in a variety of in vitro and ex vivo preparations (21–24). Based on this past work in reduced preparations, we hypothesized that *Syngap1* regulates experience-dependent ensemble plasticity by promoting the strengthening of excitatory synapses within functional cortical networks. We found that *Syngap1* was required for spike-timing-dependent (STD) synaptic potentiation and experience-mediated synapse bouton formation in layer (L) 2/3 of somatosensory cortex (SSC) but not synaptic depression or synapse bouton elimination. *Syngap1* heterozygosity in mice disrupted experience-dependent potentiation of neuronal activity within a subpopulation of L2/3 SSC neurons. *Syngap1* loss of function had no effect on plasticity of neurons within the same ensemble that weakens with experience. These findings indicate that disruptions to synapse-level strengthening mechanisms in *Syngap1* mice contribute to imbalanced cortical ensemble plasticity driven by novel sensory experience. We propose that a key function of *Syngap1* is to promote complex network-level plasticity through the strengthening of excitatory connections within cortical circuits.

Results

***Syngap1* Regulates Both Functional and Structural Excitatory Synapse Plasticity in Cortical Circuits.** Hebbian plasticity of excitatory synapses in upper lamina of SSC is believed to be a physiological mechanism for cortical map plasticity during sensory experience (7, 10, 25). While *Syngap1* is known to regulate LTP in CA1 of the hippocampus, its role in cortical STD plasticity, a form of synaptic plasticity engaged by experience within cortical circuits, is unknown. To evaluate the role of *Syngap1* in this type of cortical synapse plasticity, we prepared SSC-containing thalamocortical ex vivo slices from *Syngap1*$^{+/+}$ and *Syngap1*$^{+/-}$ mice. We induced STD plasticity by precisely pairing L4 electrical stimulation with L2/3 neuron spiking (Fig. 1*A*). STD-LTP in L2/3 neurons was reliably induced in slices produced from *Syngap1*$^{+/+}$ animals but not in slices produced from *Syngap1*$^{+/-}$ littermates (Fig. 1 *B–D*). The role of *Syngap1* in STD plasticity was restricted to potentiation because STD long-term depression was not different between genotypes (Fig. 1 *E* and *F*). Control experiments ruled out the possibility of running down of stimulation in *Syngap1*$^{+/-}$ mice because plasticity was not observed in any genotype when excitatory postsynaptic potentials (EPSPs) were elicited without postsynaptic spikes during the pairing period (Fig. 1 *G* and *H*).

Hebbian strengthening of excitatory synapses is accompanied by pre- and postsynaptic structural plasticity. Thus, we hypothesized that structural plasticity of presynaptic inputs onto L2/3 neurons, the cells with deficient STD-LTP (Fig. 1), would be impaired in *Syngap1* mice. To test this idea in vivo, *Syngap1*$^{+/-}$ mice were crossed with Thy1-eGFP mice (26) to enable repeated imaging of the same axons within L2/3 of primary somatosensory cortex (S1) before and after sensory experience (Fig. 2 *A* and *B*). Importantly, this model expresses eGFP in a subset of cortical glutamatergic neurons, which enabled us to measure plasticity of excitatory inputs within L2/3 of S1 cortex. Intrinsic optical signal (IOS) imaging was employed to identify the β whisker receptive area within S1 of each mouse (Fig. 2*B*). Two-photon imaging was performed within L2/3 of the β receptive field during baseline sessions (no trimming) and sessions occurring after the initiation of single whisker experience (SWE), where all but one whisker was trimmed on the facepad (Fig. 2 *A* and *B*). As previously described for L1 in wild-type (WT) mice (27, 28), most axonal boutons visualized in L2/3 were stable during baseline sessions, and there was no effect of genotype on bouton stability during this period (Fig. 2 *C* and *D*). Thus, *Syngap1* loss of function did not inherently disrupt axonal bouton stability. SWE increased the turnover rate (TOR) of synaptic boutons in *Syngap1*$^{+/+}$ mice (Fig. 2 *C* and *E*), which reflects a form of structural plasticity driven by sensory experience. In contrast, TOR decreased in *Syngap1*$^{+/-}$ mice in response to SWE (Fig. 2 *C* and *E*). Consistent with opposing effects of SWE on TOR, we observed a large genotype effect in this measure during trimming sessions. The genotype effect for TOR was largely driven by alterations to SWE-induced synaptic bouton formation in *Syngap1*$^{+/-}$ mice. While bouton formation rate increased in *Syngap1*$^{+/+}$ mice in response to SWE, it decreased in *Syngap1*$^{+/-}$ mice (Fig. 2*F*). In contrast, there was no change in the elimination rate in either genotype in response to SWE (Fig. 2*G*). These data demonstrate that experience-driven structural plasticity of excitatory inputs onto L2/3 S1 neurons is disrupted by *Syngap1* heterozygosity.

***Syngap1* Regulates Response Plasticity of Distinct Neuronal Subpopulations within Sensory-Evoked Cortical Ensembles.** Our data demonstrate that *Syngap1* heterozygosity disrupts synapse plasticity mechanisms required to strengthen excitatory connections in cortical circuits. We next sought to understand how disruption to these mechanisms influences complex forms of network-level plasticity, such as experience-dependent changes in cortical ensemble activity. SWE is an attractive model to study network plasticity because it triggers a redistribution of activity within neurons that comprise cortical ensembles. Individual neurons within an ensemble exhibit both increases and decreases in somatic responsiveness following sensory experience. Thus, measuring experience-dependent plasticity of individual neurons that comprise a cortical ensemble may help to connect the role of *Syngap1* at synapses to more complex forms of network plasticity. To do this, we crossed *Syngap1*$^{+/-}$ mice (21, 29) to a mouse line that stably expresses the Thy1-GCaMP6s transgene (GP4.3) (30). This strategy enabled longitudinal somatic activity measurements of the exact same SSC L2/3 neuronal population before and after SWE (Fig. 3*A*). We measured GCAMP6 signal dynamics within the perisomatic region of visually identified neurons. Dynamics from the soma result from calcium influx occurring in response to action potential (AP) firing. Small signals (~10 to 20% dF/F) reflect low levels of electrical activity, such as isolated APs, whereas larger signals (>100% dF/F) are suggestive of AP bursting (30). In each animal, we identified two distinct whisker receptive areas of cortex by IOS, such as β and C2. However, before tracking changes to cortical population responses during SWE, it is important to confirm that neuronal ensembles are stable across multiple baseline (e.g., pretrimming) sessions. Therefore, we first assessed the stability of sensory-evoked ensembles during "baseline" sessions in both genotypes. Population responses of L2/3 neurons imaged from both receptive areas were combined to assess overall stability of evoked ensembles. Individual cortical neurons demonstrated substantial response variability between imaging sessions in both genotypes. However, the two populations as a whole each appeared stable across multiple baseline sessions in each genotype (Fig. 3 *B* and *C*). Stability was defined as the average change in activity across all responsive neurons within genotype not significantly differing from "0" (*Syngap1*$^{+/+}$ versus "0," Wilcoxon

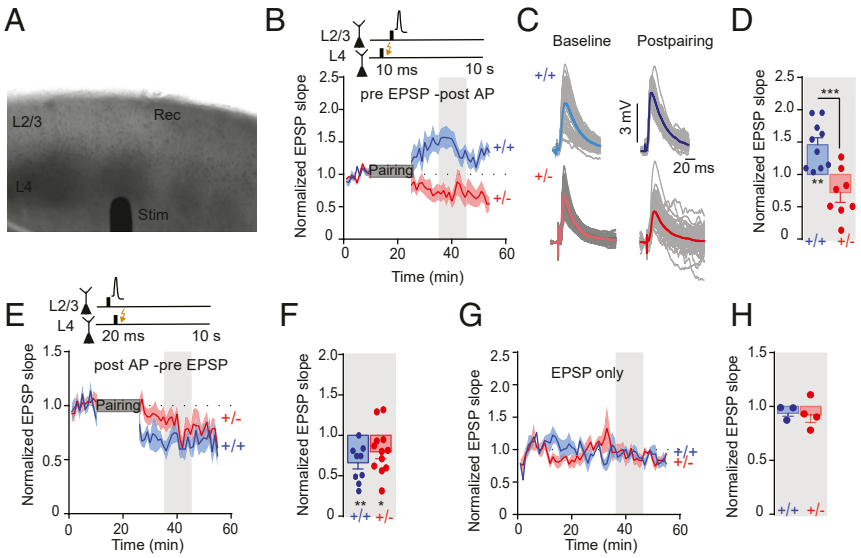

Fig. 1. *Syngap1* is required for STD-LTP, but not depression, in L2/3 sensory cortex neurons. (*A*) Image showing L4 barrels, position of stimulation electrode, and recording electrode in wS1-containing thalamocortical slice. (*B*) Induction of STD-LTP in wS1 L2/3 neurons in *Syngap1*$^{+/+}$ (n = 10 cells from 8 animals; 6 male and 2 female mice) and *Syngap1*$^{+/-}$ mice (n = 9 from 6 animals; 4 male and 2 female mice). The shaded area represents the time points where the quantification was performed. (*C*) Representative traces showing EPSPs before (baseline) and after (plasticity) the induction of STD-LTP in *Syngap1*$^{+/+}$ and *Syngap1*$^{+/-}$ mice. (*D*) Change in EPSP slope after STD-LTP induction in *Syngap1*$^{+/+}$ (n = 10 cells from 8 mice; one-sample t test, $t_9 = 4.048$, $P = 0.0029$) and *Syngap1*$^{+/-}$ mice (n = 8 cells from 6 mice; one-sample t test, $t_7 = 2.307$, $P = 0.0544$; unpaired t test, $t_{16} = 4.41$, $P = 0.0004$). (*E*) Induction of STD-LTD in wS1 L2/3 neurons in *Syngap1*$^{+/+}$ (n = 9 neurons from 5 mice; 3 male and 2 female mice) and *Syngap1*$^{+/-}$ mice (n = 12 neurons from 8 mice; 6 male and 2 female mice). The shaded area represents the time points where the quantification was performed. (*F*) Change in EPSP slope after STD-LTD induction in *Syngap1*$^{+/+}$ (n = 9 cells from 5 mice; one-sample t test, $t_8 = 4.375$, $P = 0.0024$) and *Syngap1*$^{+/-}$ mice (n = 12 neurons from 8 mice, one-sample t test, $t_{11} = 2.418$, $P = 0.0341$). (*G*) Control experiments in which only EPSP were evoked during the pairing period (n = 3 *Syngap1*$^{+/+}$ neurons from 3 mice; n = 4 *Syngap1*$^{+/-}$ mice neurons from 2 mice). The shaded area represents the time points where the quantification was performed. (*H*) Change in EPSP slope in control experiments (n = 3 *Syngap1*$^{+/+}$ neurons from 3 male mice; n = 4 *Syngap1*$^{+/-}$ neurons from 2 male mice). Bars represent mean ± SEM; $*P \leq 0.05$, $**P \leq 0.01$, and $***P \leq 0.001$.

signed-rank test, $P = 0.071$; *Syngap1*$^{+/-}$ versus "0," Wilcoxon signed-rank test, $P = 0.236$). Even though the complete populations did not significantly change activity across baseline sessions as measured by the one-sample within-genotype comparison, there was a weak effect when we compared changes in activity between genotypes. This appears to be driven by subtle, but opposing, nonsignificant trends in population activity changes in each genotype. Next, as done previously (8), the global neuronal population was subdivided into three subpopulations based on response amplitude during a baseline session (i.e., low active, 63.3%; medium active, 29.6%; high active, 7.1%; Fig. 3*B*). We continued to observe stability within the subpopulations in both *Syngap1*$^{+/+}$ (Fig. 3*D* and *SI Appendix*, Table S1) and *Syngap1*$^{+/-}$ mice (Fig. 3*E* and *SI Appendix*, Table S1) as noted by the lack of significant effects in the one-sample within-genotype comparisons. There was a genotype effect in the high-activity population but not in the others, even though each population was not changed from "0" in this group of neurons. Similar to what was observed for the complete population (Fig. 3*C*), the genotype effect in the high-activity neurons appears driven by opposing nonsignificant shifts in activity.

The baseline stability of the SSC neuronal ensembles, as well as the three subpopulations that comprise them, permitted an analysis of how activity of these neurons changed in response to SWE (Fig. 4*A*). We first measured SWE-induced population-level changes in a spared cortical area (Fig. 4*B*). We identified a cortical ensemble within the spared area that was evoked by deflection of a trimmed whisker. By comparing the amplitude of each neuron before and after SWE, we were able to measure response plasticity for each neuron in the ensemble. In *Syngap1*$^{+/+}$ mice, there was no change in average activity across the ensemble in response to SWE (Fig. 4*C*). While many neurons increased or decreased activity in response to SWE, the average change across the ensemble was not different compared to preexperience levels, indicating that total activity within this ensemble was stable in response to experience. In contrast, the average SWE-induced ensemble response was decreased in *Syngap1*$^{+/-}$ mice relative to preexperience baseline levels (Wilcoxon signed-rank test, $P = 0.0003$). Consistent with this, we observed that global ensemble plasticity was different between genotypes (Fig. 4*C*), demonstrating that *Syngap1* regulates cortical neuron ensemble plasticity induced by SWE.

To gain insight into how *Syngap1* heterozygosity disrupted experience-dependent ensemble plasticity in sensory cortex, we group neurons within the ensemble into three subpopulations based on somatic activity during baseline sessions (low activity, medium activity, and high activity). In response to SWE, "low activity" neurons residing in the spared cortical area displayed significant potentiation in response to nonprincipal whisker (NPW; trimmed) stimulation in *Syngap1*$^{+/+}$ mice (Fig. 4*D*). In contrast, spatially intermingled "high activity" neurons significantly decreased their responses to the same whisker stimulation (Fig. 4*D* and *SI Appendix*, Table S1), a finding in agreement with previous studies (8). Medium-activity neurons exhibited the most stability of the three subpopulations. In *Syngap1*$^{+/-}$ mice, high-activity neurons also scaled down their activity (Fig. 4*D* and *SI Appendix*, Table S1) and as a group, was not different to the same subpopulation measured in *Syngap1*$^{+/+}$ mice (Fig. 4*D*). Similarly, response plasticity in the medium-activity population was stable, and no differences were observed compared to corresponding neurons from *Syngap1*$^{+/+}$ mice. However, there was a noticeable reduction in plasticity within the low-activity population in *Syngap1*$^{+/-}$ mice. Consistent with this observation, plasticity within this subpopulation was significantly reduced compared to *Syngap1*$^{+/+}$ mice. Furthermore, we observed nearly identical results when sensory responses were evoked through deflection of the principal whisker (PW) (Fig. 4*E*). Analysis of the combined ensemble demonstrated a strong effect of genotype (Fig. 4*F*). In addition, neurons from *Syngap1*$^{+/-}$ mice were biased toward weakening of activity (Wilcoxon signed-rank test, $P = 0.0279$).

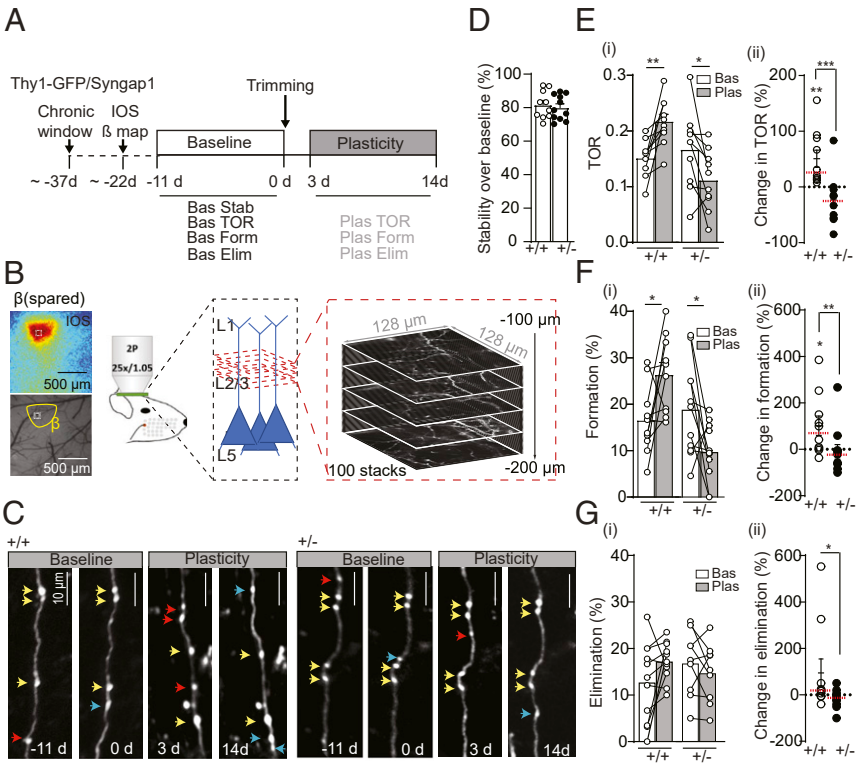

Fig. 2. *Syngap1* heterozygosity disrupts experience-dependent presynaptic bouton dynamics in L2/3 sensory cortex. (*A*) Experimental timeline. Thy1-GFP/*Syngap1*$^{+/+}$ or Thy1-GFP/*Syngap1*$^{+/-}$ mice were implanted with a chronic cranial window and recovered for at least 2 wk before IOS imaging. IOS was used to identify the cortical location activated by the deflection of the β whisker. After two baseline two-photon sessions were performed, whiskers were trimmed (all contralateral whiskers but β) every 2 d, and animals were imaged for two more sessions. (*B*) Representation of in vivo imaging procedure of axonal bouton segments in wS1 L2/3 in Thy1-GFP/*Syngap1* mice. (*C*) Images obtained in different baseline and plasticity sessions showing axonal dynamics in *Syngap1*$^{+/+}$ and *Syngap1*$^{+/-}$ mice. Yellow arrows indicate stable axonal boutons blue arrows indicate new boutons, and red arrows indicate lost boutons. (*D*) Bouton stability over baseline sessions in *Syngap1*$^{+/+}$ and *Syngap1*$^{+/-}$ mice. (*E*, *i*) Axonal bouton TOR before and after SWE in *Syngap1*$^{+/+}$ (paired *t* test, $t_9 = 4.08$, $P = 0.0028$; $n =$ 10 mice) and *Syngap1*$^{+/-}$ mice (paired *t* test, $t_9 = 2.735$, $P = 0.0230$; $n = 10$ mice). (*ii*) Change in TOR in *Syngap1*$^{+/+}$ (one-sample *t* test, $t_9 = 3.272$, $P = 0.0096$; $n =$ 10 mice) and *Syngap1*$^{+/-}$ mice (Wilcoxon signed-rank test, $P = 0.0977$; $n = 10$ mice; Mann–Whitney *U* test, $U = 7.00$, $P = 0.0005$). (*F*, *i*) Percentage of axonal bouton formation before and after SWE in *Syngap1*$^{+/+}$ (paired *t* test, $t_9 = 2.59$, $P = 0.0294$; $n = 10$ mice) and *Syngap1*$^{+/-}$ mice (paired *t* test, $t_{10} = 2.321$, $P =$ 0.0427; $n = 11$ mice). (*ii*) Change in axonal bouton formation in *Syngap1*$^{+/+}$ (one-sample *t* test, $t_9 = 2.42$, $P = 0.0383$; $n = 10$ mice) and *Syngap1*$^{+/-}$ mice ($n = 11$ mice; Mann–Whitney *U* test, $U = 18.00$, $P = 0.0078$). (*G*, *i*) Percentage of axonal bouton elimination before and after SWE in *Syngap1*$^{+/+}$ ($n = 10$ mice) and *Syngap1*$^{+/-}$ mice ($n = 10$ mice). (*ii*) Change in axonal bouton elimination in *Syngap1*$^{+/+}$ ($n = 10$ mice) and *Syngap1*$^{+/-}$ mice ($n = 10$ mice; Mann–Whitney *U* test, $U = 23.00$, $P = 0.0433$). Data obtained from a total of 549 boutons in *Syngap1*$^{+/+}$ mice and 478 boutons in *Syngap1*$^{+/-}$ mice. For *Syngap1*$^{+/+}$, seven female and three male mice were used. For *Syngap1*$^{+/-}$, five female and six male mice were used. Bars represent mean or mean ± SEM. Medians are represented by red or black dashed lines. Circles are animal means. $*P \leq 0.05$, $**P \leq 0.01$, and $***P \leq 0.001$.

When looking at specific neuronal subpopulations, we again observed both increases and decreases in neuronal responsiveness across the ensemble in each genotype (Fig. 4*G*). However, the only subpopulation with a genotype effect was again within the low-active population (Fig. 4*G*), where plasticity was significantly reduced in the mutants compared to WT controls.

***Syngap1*-Mediated Regulation of Ensemble Plasticity Is Linked to a Dynamic Process Unrelated to Developmental Critical Periods.** We hypothesized that *Syngap1* regulates experience-dependent changes in cortical population activity by initiating dynamic cellular processes that promote synaptic strengthening. However, it is also possible that alterations in the development of whisker S1 (wS1) circuits may contribute to these observations (31). We reasoned that if SynGAP protein controlled dynamic cellular processes, such as experience-dependent synapse strengthening, then reexpressing this protein in adult *Syngap1* mutant animals (i.e., after neuronal development is complete) should improve ensemble plasticity driven by SWE. To test this, we performed repeated GCaMP6s imaging in the same neuronal populations from *Syngap1*$^{+/lx\text{-}st}$/Cre-ER/Thy1-GCaMP6s mice treated with either vehicle or tamoxifen (TMX). We have extensively validated the *Syngap1*$^{+/lx\text{-}st}$/Cre-ER model in previous studies (29, 32, 33). These animals are haploinsufficient for *Syngap1* (e.g., express half the expected SynGAP protein), and TMX injections at postnatal day (PND) 60 quickly reactivate the disrupted *Syngap1* allele leading to restoration of SynGAP protein to endogenous levels. The overall design of this study was similar to that of Fig. 4*A*, except that *Syngap1*$^{+/lx\text{-}st}$/Cre-ER/Thy1-GCaMP6s mice were used and injected with either vehicle or TMX at PND60 (Fig. 5*A*). Importantly, TMX injections were performed ∼1 mo before ensemble imaging and initiation of whisker trimming. Thus, the brain was clear of TMX for several weeks before the onset of data collection. TMX injections significantly increased SynGAP protein expression (*SI Appendix*, Fig. S1*A*). Thus, during data collection at PND ∼90 (*SI Appendix*, Fig. S1*B* and Fig. 5*A*), vehicle-treated mice were *Syngap1* mutants, while TMX treatment converted mice to the genetic equivalent of WT animals. During baseline imaging sessions (*SI Appendix*, Fig. S1*B*), the average change in somatic responses from the entire ensemble was stable, with no differences between genotypes (*SI Appendix*, Fig. S1*C*). Neurons were then grouped into three subpopulations based on baseline response amplitude. The average change in responsivity

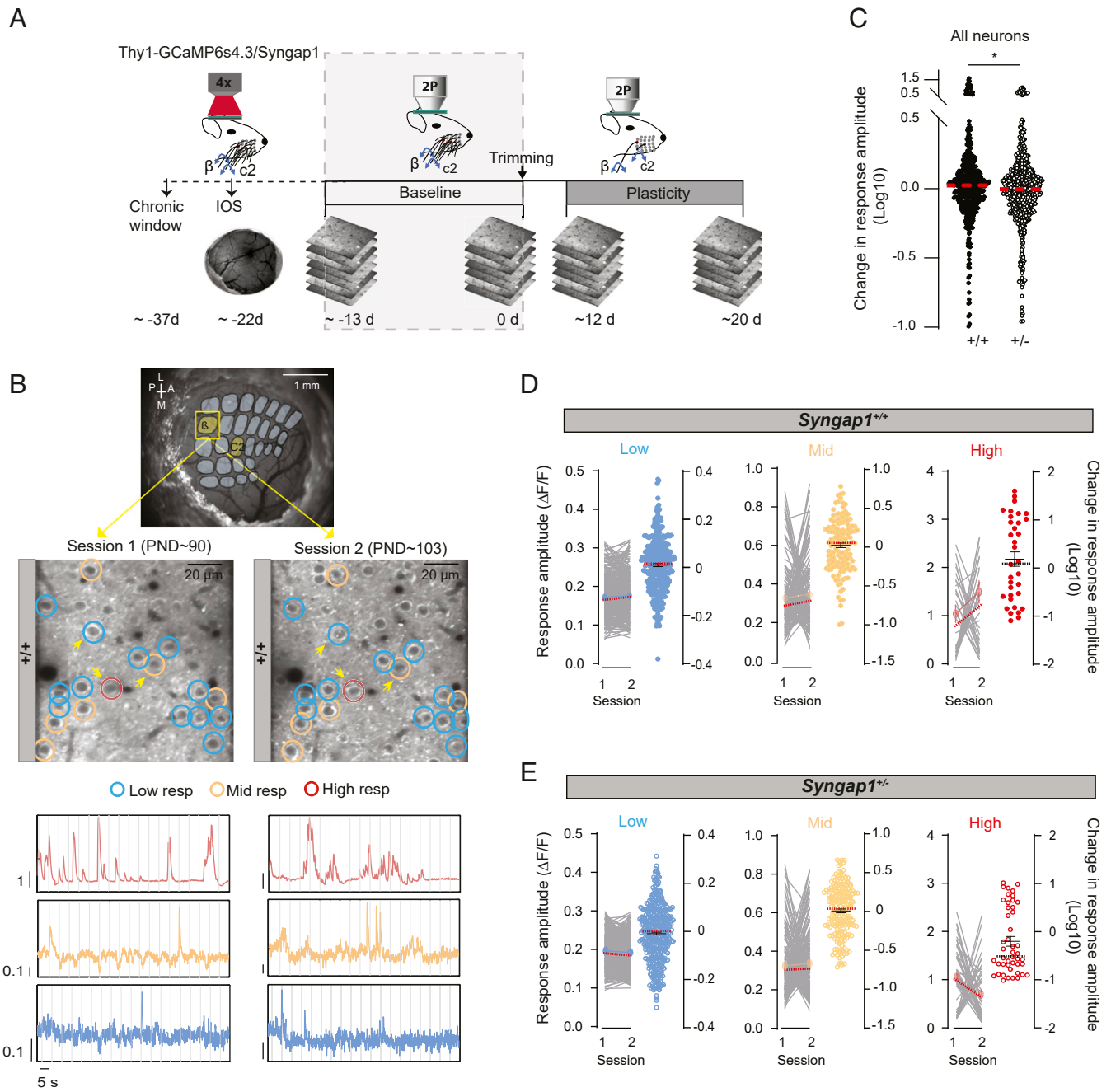

Fig. 3. Stable whisker responsiveness of L2/3 cortical ensembles during baseline (no trimming) imaging sessions. (*A*) Experimental timeline/design. Thy1-Gcamp6s4.3/*Syngap1*$^{+/+}$ and Thy1-Gcamp6s4.3/*Syngap1*$^{+/-}$ mice were implanted with a chronic cranial window and allowed to recover for at least 2 wk before IOS imaging. IOS was used to identify the locations activated by the deflection of the PW and NPW or β and C2 whiskers, respectively. Baseline imaging sessions (gray shaded region) were carried out ∼−13 and 0 d before whisker trimming (i.e., day 0). (*B*) Image of cortical surface (*Top*) through a chronic cranial window with an overlaid barred field, imaging areas indicated in yellow (β and C2). Representative in vivo two-photon microscopy images and representative ΔF/F traces (*Bottom*) from the same cells of a *Syngap1*$^{+/+}$ mouse over two baseline imaging sessions. Circles show low- (blue), mid- (beige), and high- (red) active cells. (*C*) Change in response amplitude over two baseline sessions for all cells from both β and C2 receptive areas over two baseline sessions in *Syngap1*$^{+/+}$ (n = 483 cells from 4 mice) and *Syngap1*$^{+/-}$ mice (n = 654 cells from 6 mice; Mann–Whitney U test, U = 146,097, P = 0.0305). (*D* and *E*) Response amplitude and change in response amplitude for each cell class from both β and C2 receptive areas over two baseline sessions in *Syngap1*$^{+/+}$ (*D*) and *Syngap1*$^{+/-}$ mice (*E*) (n = 306 low-active cells, n = 143 mid-active cells, n = 34 high-active cells from 4 *Syngap1*$^{+/+}$ mice; n = 414 low-active cells, n = 194 mid-active cells, n = 46 high-active cells from 6 *Syngap1*$^{+/-}$ mice). For Syngap1$^{+/+}$, one female and three male mice were used. For Syngap1$^{+/-}$, one female and five male mice were used. Medians are represented by red or black dashed lines. Circles are individual cell values or cell class mean values. *$P \leq 0.05$.

from each subgroup was also generally stable across baseline imaging sessions (*SI Appendix*, Fig. S1 *D* and *E*). The exception was the high-activity population in *Syngap1* rescue animals (+TMX; *SI Appendix*, Fig. S1*E*), which demonstrated a slight, but significant, shift toward increased activity during the baseline period. This may reflect a prolonged homeostatic adaptation of the cortical network in response to reexpression of SynGAP protein, which occurred at the time of TMX injections, or several weeks prior the

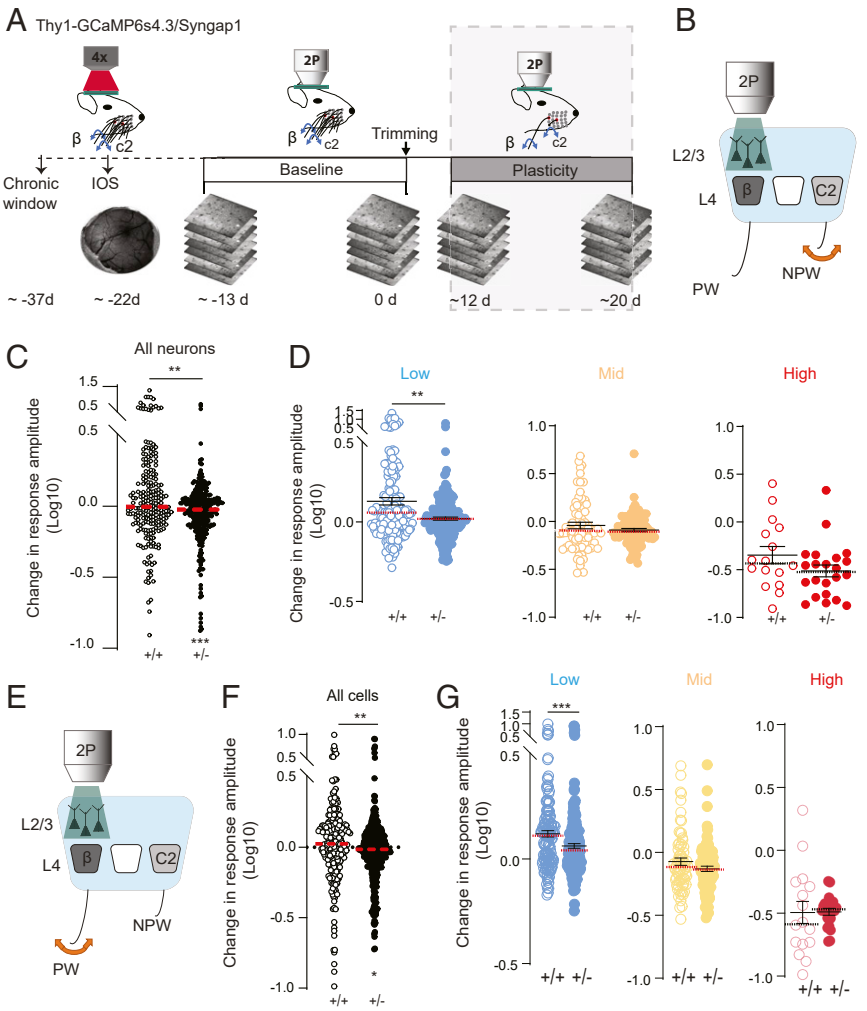

Fig. 4. *Syngap1* heterozygosity disrupts experience-dependent cortical ensemble plasticity. (*A*) Experimental timeline/design—continued from Fig. 3. To induce SWE, whiskers were trimmed (all contralateral whiskers but PW) every 2 d, and animals were imaged for two more sessions at day ~12 and ~20 after trimming (gray shaded region). (*B*) Representation of the experimental design consisting of deflecting the trimmed/NPW and imaging in the spared/PW wS1. (*C*) Change in response amplitude (the ratio of plasticity/baseline) for the trimmed/NPW stimulation for all cells in the spared wS1 in *Syngap1*$^{+/+}$ (n = 230 cells from 4 mice) and *Syngap1*$^{+/-}$ mice (n = 307 cells from 6 mice; Wilcoxon signed-rank test, P = 0.0003; Mann–Whitney U test, U = 30,073, P = 0.0033). (*D*) Change in response amplitude (the ratio of plasticity/baseline) for the trimmed/NPW stimulation for each cell class in the spared wS1 in *Syngap1*$^{+/+}$ (n = 146 low-active cells, n = 68 mid-active cells, n = 16 high-active cells from 4 mice) and *Syngap1*$^{+/-}$ mice (n = 194 low-active cells, n = 91 mid-active cells, n = 22 high-active cells from 6 mice; Mann–Whitney U test, U = 11,532, P = 0.0034). (*E*) Representation of the experimental design consisting of deflecting the spared/PW and imaging in the spared wS1. (*F*) Change in PW-response amplitude after SWE for cells in the spared wS1 in *Syngap1*$^{+/+}$ (n = 230 neurons from 4 mice) and *Syngap1*$^{+/-}$ mice (n = 307 neurons from 6 mice; Wilcoxon signed-rank test, P = 0.0279; Mann–Whitney U test, U = 29,680, P = 0.0016). (*G*) Change in PW-response amplitude after SWE for each cell class in the spared wS1 of *Syngap1*$^{+/+}$ (n = 145 low-active cells, 69 mid-active cells, 16 high-active cells from 4 mice; Mann–Whitney U test, U = 10,837, P = 0.0002) and *Syngap1*$^{+/-}$ mice (n =195 low-active cells, 91 mid-active cells, 21 high-active cells from 6 mice). For Syngap1$^{+/+}$, one female and three male mice were used. For Syngap1$^{+/-}$, one female and five male mice were used. Medians are represented by red or black dashed lines. Circles are individual cell values. (*$P \leq 0.05$, **$P \leq 0.01$, ***$P \leq 0.001$.)

onset of baseline imaging. During SWE, responsiveness of the global ensemble in vehicle-treated mice was shifted toward less activity (Fig. 5 *B*, *D*, *E*, *G*, and *H*; Wilcoxon signed-rank test, P = 0.0033 for vehicle-treated *Syngap1*$^{+/lx\text{-}st}$ rescue mice in Fig. 5*E*; Wilcoxon signed-rank test, P = 0.003 for vehicle-treated *Syngap1*$^{+/lx\text{-}st}$ rescue mice in Fig. 5*H*). This result is consistent with global ensemble response plasticity during SWE in *Syngap1*$^{+/-}$ mice (Fig. 4 *C* and *F*), which was also shifted toward less activity. Because vehicle-treated *Syngap1*$^{+/lx\text{-}st}$ also have reduced SynGAP expression, these data strengthen the interpretation that *Syngap1* expression is required for balanced cortical ensemble plasticity. In contrast, global ensemble activity was not shifted in TMX-treated *Syngap1*$^{+/lx\text{-}st}$ rescue mice (Fig. 5 *C*, *D*, *E*, *G*, and *H*), which is a result consistent with our prior observations in WT mice (Fig. 4 *C* and *F*).

We next measured SWE-mediated response plasticity from the ensemble subpopulations. A pronounced lack of experience-dependent up-regulation of somatic GCaMP6s responses was observed in the low-activity population in vehicle-treated *Syngap1* mutant mice (Fig. 5 *B*, *D*, *F*, *G*, and *I*). However, down-regulation of the high-activity population occurred normally in these mice (Fig. 5 *B*, *D*, *F*, *G*, and *I*). Because *Syngap1*$^{+/lx\text{-}st}$ animals are a distinct strain expressing haploinsufficiency for *Syngap1*, the findings in the low-activity population are again consistent with observations made previously in conventional *Syngap1*$^{+/-}$/ Thy1-GCaMP6s mice (Fig. 4 *D* and *G*). TMX-treated mice exhibited enhanced response plasticity exclusively in the low-activity population compared to vehicle-treated mice (Fig. 5 *C*, *D*, *F*, *G*, and *I*). TMX treatments had no effect on the

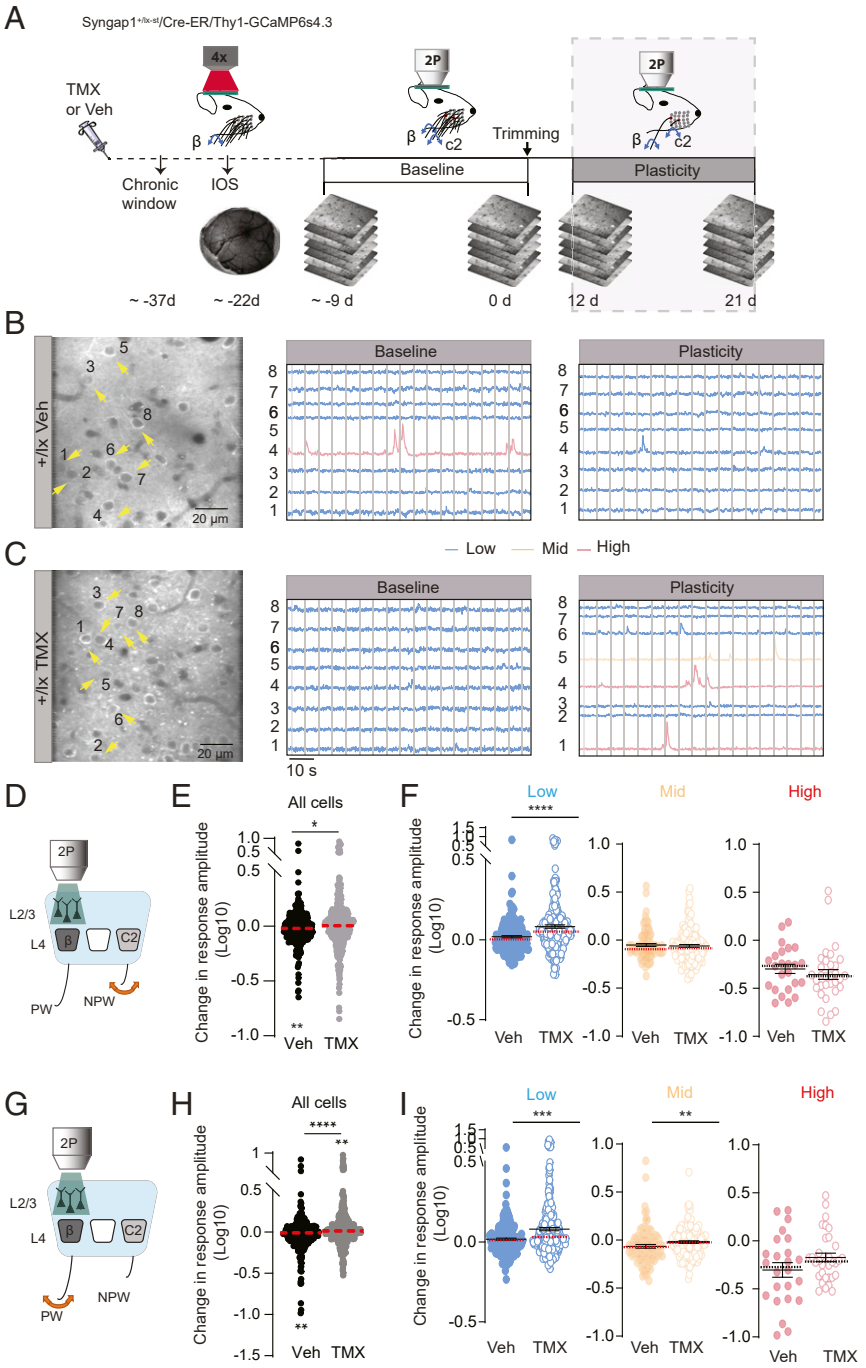

Fig. 5. TMX, given in adulthood, restores experience-dependent cortical ensemble plasticity in a *Syngap1* reexpression mouse model. (*A*) Experimental timeline. *Syngap1*$^{+/lx\text{-}st}$/Cre-ER/Thy1-GCaMP6s mice were IP injected with TMX or vehicle (Veh) and 30 d later were implanted with a chronic cranial window and allowed to recover for at least 2 wk before IOS imaging. IOS was used to identify the cortical locations activated by the deflection of the PW. Whiskers were trimmed (all but the PW) every 2 d, and animals were imaged in the spared area of wS1 over two additional sessions (gray shaded region). (*B* and *C*) Representative in vivo two-photon microscopy images from L2/3 neurons of the spared area of wS1 in (*B*) Veh-treated and (*C*) TMX-treated mice and representative ΔF/F traces from the same cells as in images before (baseline) and after SWE. Arrows indicate cells with traces shown on the *Right*. (*D*) Representation of the experimental design consisting of deflecting the trimmed/NPW and imaging in the spared wS1. (*E*) Change in trimmed/NPW-response amplitude of all cells after SWE for the spared wS1 in Veh-treated ($n = 344$ neurons from 5 mice; Wilcoxon signed-rank test, $P = 0.0033$) and TMX-treated mice ($n = 447$ neurons from 6 mice; Mann–Whitney U test, $U = 68{,}786$, $P = 0.011$). (*F*) Change in trimmed/NPW-response amplitude after SWE for each cell class in the spared wS1 of Veh-treated ($n = 218$ low-active cells, 102 mid-active cells, 24 high-active cells from 5 mice) and TMX- treated mice ($n = 283$ low-active cells, 132 mid-active cells, 32 high-active cells from 6 mice; Mann–Whitney U test, $U = 23{,}516$, $P < 0.0001$). (*G*) Representation of the experimental design consisting of deflecting the untrimmed/PW and imaging in the spared wS1. (*H*) Change in spared/PW-response amplitude after SWE for all cells in the spared wS1 in Veh-treated mice ($n = 345$ neurons from 5 mice; Wilcoxon signed-rank test, $P = 0.004$) and TMX-treated mice ($n = 460$ neurons from 6 mice; Wilcoxon signed-rank test, $P = 0.003$; Mann–Whitney U test, $U = 65{,}930$, $P < 0.0001$). (*I*) Change in spared/PW-response amplitude after SWE for each cell class in the spared wS1 of Veh-treated mice ($n = 219$ low-active cells, 102 mid-active cells, 24 high-active cells from 5 mice) and TMX-treated mice ($n = 291$ low-active cells, 136 mid-active cells, 33 high-active cells from 6 mice; low-active: Mann–Whitney U test, $U = 25{,}478$, $P = 0.0001$; mid-active: Mann–Whitney U test, $U = 5{,}523$, $P = 0.0072$). For Veh-treated mice, three females and four males were used. For TMX- treated mice, three females and three males were used. Medians are represented by red or black dashed lines. Circles are individual cell values. $^*P \le 0.05$, $^{**}P \le 0.01$, $^{***}P \le 0.001$, and $^{****}P \le 0.0001$.

medium- and high-activity neurons. This was notable given that the low-activity subpopulation was the only group significantly impacted in *Syngap1*$^{+/-}$ animals (Fig. 4 *C* and *F*). Thus, across each functional measure of somatic activity, vehicle-treated mice resembled *Syngap1*$^{+/-}$ mice, while TMX-treated mice resembled WTs.

Discussion

The reorganization of synapse structure and function is a fine-scale substrate that underlies changes in cortical population activity in response to sensory experience (7, 8, 25). However, to our knowledge, opposing functional changes within defined neuronal subpopulations of the same local cortical network during sensory experience has only been described in a single publication (8). Importantly, we confirmed many of the original findings from the Margolis et al. study (8) even though we used a distinct genetically encoded calcium sensor (GCaMP6s versus YC3.60) expressed using a different method (stably expressed transgene in the germline versus direct viral delivery to cortex). L2/3 neurons in wS1 were classified into three subpopulations based on response amplitude, and each of these populations exhibited stable levels of activity during baseline imaging sessions (i.e., no whisker trimming). This finding was critical because the analysis of population-based plasticity during SWE relies on the stability of these populations during baseline conditions. Most importantly, we replicated the key finding of the Margolis et al. study; the observation that spatially intermingled cells within SSC exhibited highly specific and sometimes opposing changes in activity during SWE (8). We observed opposing changes in responsiveness of different types of functionally defined cortical neurons within the same imaging fields in SSC. Neurons defined as "low activity" increased responses in response to SWE, while "high activity" neurons exhibited reduced sensory responsiveness during trimming sessions. Margolis et al. argued that the differences observed in these subpopulations emerged from their distinct role within the barrel cortex network (8). Low-active neurons, which are most neurons in SSC, weakly respond to whisker stimulation but exhibit the largest change in response to SWE. Their ability to extensively scale-up activity is thought to enable remapping of cortical circuits in response to experience, which would change computational functions within the network. Scaling down of spatially intermingled highly active neurons may be a form of experience-dependent plasticity that balances overall firing rates within the network in the face of significantly up-regulated activity in the low-activity population. It remains unclear to what extent reduced activity in these neurons occurs through direct Hebbian synaptic weakening or indirectly through homeostatic readjustments within the broader cortical microcircuit. Alternatively, scaling down of the high-activity population could arise through neuronal toxicity from exogenous expression of calcium sensors, or they could represent a distinct neuronal type, such as fast-spiking interneurons. Our studies argue against these two alternative possibilities. Neuronal toxicity in the GP4.3 transgenic mouse line has been documented to be minimal (30). Indeed, stable neuronal responses have been reported over the course of many months in this mouse line. In our experiments, we observed very few cells with nuclear GCAMP6 expression, a marker of neuronal toxicity, even after 3 mo of experimentation with up to six repeated imaging sessions in the same cortical fields of view. In addition, within the cortex, GCaMP6 is not expressed in GABAergic neurons (30). Therefore, both low- and high-activity populations were comprised exclusively of glutamatergic neurons, demonstrating that neighboring neurons of the same general type (e.g., excitatory projections neurons) can exhibit opposing changes in neuronal responsiveness as a consequence of SWE.

Our findings in *Syngap1* mutant models support the idea that distinct molecular and cellular mechanisms underlie subpopulation-specific changes to neuronal activity during SWE. Indeed, *Syngap1* effects on ensemble plasticity were limited to the low-activity subpopulation. We found that SWE-mediated scaling up of the low-active wS1 neuronal subpopulation was impaired in two distinct models of *Syngap1* haploinsufficiency [*Syngap1*$^{+/-}$ (Fig. 4) and *Syngap1*$^{+/tx\text{-}st}$ animals (Fig. 5)]. However, plasticity of the highly active subpopulation, which scale-down their activity during whisker experience, was unimpaired in these two mutant strains. Thus, expression of *Syngap1* promotes neuron-specific plasticity within whisker-responsive sensory cortex ensembles. Several lines of evidence indicate that *Syngap1* promotes experience-dependent scaling up of low-active neurons through the regulation of cellular mechanisms that strengthen excitatory synaptic connections in L2/3 SSC. Similar to past reports (27, 28), we found that whisker experience triggered axonal dynamics resulting in a net gain of new synaptic boutons in upper lamina cortex of WT mice. Thy1-eGFP mice used in this study express the fluorescent reporter exclusively within excitatory neurons (26), demonstrating that there was a net gain of excitatory input in L2/3 in response to whisker trimming. This is a plausible mechanism contributing to scaling up of the low-activity population during whisker experience. In *Syngap1* mutant mice, however, whisker experience caused a reduction, rather than an increase, in the formation of new boutons. Thus, losing one copy of *Syngap1* prevented a form of experience-dependent structural plasticity that drives a net gain of excitation within upper lamina SSC circuits. In addition to disrupted experience-dependent synapse structural plasticity, we also observed impaired functional plasticity of L2/3 SSC excitatory synapses in *Syngap1* mice. STD-LTP in acute brain slices obtained from *Syngap1* mutants was absent in barrel cortex L2/3 neurons. This form of LTP is thought to contribute to whisker map expansion of the spared whiskers (25, 34). Importantly, we found that low-active neurons in the deprived area of wS1 from *Syngap1* mice failed to scale-up activity in response to stimulation of the spared whisker, a finding consistent with impaired STD-LTP.

These observations in cortical circuits are consistent with known functions of SynGAP protein in hippocampal neurons. SynGAP protein is a core constituent of the postsynaptic density within dendritic spines where it dynamically regulates small GTPase signaling in an NMDA receptor and CAMKII-dependent manner to regulate AMPAR trafficking required for synapse strengthening (17, 20). Our data also indicate that synaptic weakening mechanisms are intact in SSC of *Syngap1* mice. Axonal bouton elimination rates and STD-LTD were not different between genotypes in L2/3 of wS1. This is consistent with known hippocampal functions of SynGAP, where synaptically evoked LTD at Schaeffer collaterals in *Syngap1* mutants is unimpaired (21). The observation here that *Syngap1* heterozygosity disrupts synapse strengthening mechanisms in cortex, while leaving weakening mechanisms intact, may explain how global ensemble activity was consistently reduced after whisker experience (Fig. 4 *C* and *F*, *Syngap1*$^{+/-}$ animals; Fig. 5 *E* and *H*, vehicle animals). In addition to effects on dendritic spine synapse function, *Syngap1* heterozygosity can also impact inhibitory synapses in cortical microcircuits (35). Therefore, it is also possible that selective impairments in scaling up of low-activity neuronal population in *Syngap1* mice arises through dysfunction of GABAergic inhibitory synapses in response to whisker experience. While our data demonstrate that functionally distinct subpopulations of excitatory neurons express differing forms of plasticity in response to experience, additional experiments will be required to identify the direct impacts of *Syngap1* expression within excitatory versus inhibitory microcircuit elements. Regardless, based on our current findings, it is reasonable to propose that experience-dependent ensemble plasticity is balanced by competing genetic mechanisms. These competing genetic mechanisms are likely engaged in a cell-specific manner, enabling some neurons to increase activity and others to decrease activity in response to experience. In the case of *Syngap1* heterozygous mice, this balance is compromised by the loss of an essential synapse strengthening mechanism. Weakening mechanisms are left to dominate during whisker experience in these

mice, which can lead to an overall weakening of the global ensemble (Figs. 4 *C* and *F* and 5 *E* and *H*).

Experiments with adult TMX injections in the *Syngap1* reexpression mouse model suggest that disruption to ensemble plasticity in mutant animals is not due to an impaired developmental process. Rather, restoration of experience-dependent ensemble plasticity within low-activity L2/3 neurons in TMX-injected mice supports a model where SynGAP protein controls dynamic cellular processes, initiated at the time of experience, to support the redistribution of neuronal population activity. These dynamic processes are likely comprised of activity-dependent strengthening of excitatory connections within the whisker responsive network. Past studies on *Syngap1* biology support the interpretation that the control of this gene over synapse plasticity is not restricted to development. To the contrary, SynGAP appears to exert control over activity-dependent strengthening of synapses throughout life. For example, impaired Schaffer collateral LTP in *Syngap1* mutant mice is completely rescued after adult reexpression of SynGAP protein (22). Importantly, dynamic Ras/ERK signaling initiated by theta-burst stimulation was also rescued in the adult hippocampus of *Syngap1* mutants in this same study. Consistent with these findings, adult reexpression of SynGAP protein also improves deficits in hippocampal theta rhythms in concert with systems memory consolidation of long-lasting contextual fear (33), which are processes that rely on intact hippocampal function and synapse plasticity (36). The adult reversal experiments in this study must be interpreted with caution. It is possible that the transient application of TMX itself may have been responsible for observed effects. For technical reasons, we were not able to completely control for off-target effects of TMX. However, there are several pieces of evidence suggesting that TMX on its own may not be responsible for improved ensemble plasticity in the rescue model. First, TMX injections occurred ∼1 mo before the commencement of imaging and whisker trimming. Thus, for TMX to cause an off-target restoration of plasticity, the compound would have had to activate a latent mechanism that was engaged more than 1 mo later to reactivate plasticity. This is unlikely given that TMX is an antagonist of estrogen receptor-mediated synapse plasticity and that TMX has been shown to disrupt Hebbian synaptic strengthening rather than enhancing it (37). Moreover, the only measures that were significantly improved in TMX-treated animals were those that were reliably disrupted in *Syngap1*$^{+/-}$ mice. TMX treatment was transient, but it triggered a permanent reactivation of SynGAP protein expression. Having said this, the very real possibility remains that TMX, rather than SynGAP protein reexpression, led to reactivation of plasticity within the low-activity neuronal population.

This current study extends our understanding of how neurodevelopmental disorders (NDD)/ASD genetic risk contributes to sensory processing impairments within cortical circuits. Our prior work in *Syngap1* mouse models demonstrated impaired touch-dependent behaviors, including impaired texture discrimination and impaired whisker-dependent adaptation of licking behavior (31). This study also presented evidence from patient populations that children with pathogenic *SYNGAP1* variants expressed abnormal behavioral responses to tactile input. Whiskers are the principal touch organ in rodents (38). Whisker-touch perceptions are shaped by cortical function, with barrel cortex serving as an area where whisker-generated signals are integrated with distinct information streams, such as other sensory modalities and current internal state (39). Therefore, it is important to understand how *Syngap1* impacts barrel cortex circuitry and function. Our prior study also reported reduced barrel cortex activation in response to whisker stimulation (31). A neurophysiological mechanism contributing to abnormal barrel cortex activation was reduced feed-forward excitation in upper lamina of these mice, which is a circuit phenotype consistent with impaired touch-dependent behaviors (40). A contributing factor to feed-forward excitation deficits in barrel cortex of *Syngap1* mice was arrested development of excitatory neurons in L2/3/4 of these mice. It is possible that other neurobiological factors may also contribute to impaired function of barrel cortex circuits in this NDD/ASD model of genetic risk. Given that sensory cortex develops through use-dependent strengthening of excitatory inputs (34), and *Syngap1* is known to regulate synaptic potentiation in reduced preparations (17, 20), the findings in this current study suggest that impaired scaling up of neural activity in response to experience during development may also contribute to deficits in barrel cortex activation in response to whisker usage. However, it remains unknown to what extent cortical circuit dysfunction causes deficits in whisker-touch processing and whisker-dependent behavioral adaptions. As a result, additional studies are required to address the cause-and-effect relationships linking cortical circuit dysfunction downstream of *Syngap1* pathogenicity and whisker-dependent behavioral deficits in these models.

Materials and Methods

Animals. All animal procedures were conducted in accordance with the NIH Guide for the Care and Use of Laboratory Animals, and all procedures were approved by the Scripps Institutional Animal Care and Use Committee (41). Males and females were used in all experiments and final male/female ratio in datasets reflect uncontrollable variables, such as the ratio of male/female (M/F) offspring achieved from the multigenerational breeding schemes and experimental attrition. Mice were housed four or five per cage on a 12-h normal light–dark cycle. For experiments requiring chronic cranial window and headpost implantation, mice were singly housed following surgery with cardboard huts for the remainder of the study. We used inbred *Syngap1* constitutive (*Syngap1*$^{+/-}$) (21) or *Syngap1* conditional rescue (*Syngap1*$^{lx\text{-}st}$) mice (29). Each line is maintained by colony inbreeding on a mixed background of C57-BL6/129s. Every seventh generation, *Syngap1*$^{+/-}$ or *Syngap1*$^{lx\text{-}st}$ mice are refreshed by crossing colony breeders into C57-BL6/129 F1 animals for one generation. Offspring from these crosses, like those used for this study, are then inbred for up to seven generations. For two-photon microscopy experiments, *Syngap1*$^{+/-}$ or *Syngap1*$^{lx\text{-}st}$ mice were crossed with Thy1-GCaMP6s4.3 (no. 024275) or Thy1-GFP (no. 007788) reporter lines, which were purchased from Jackson Laboratories. F1 offspring were used for these studies, except for animals generated for studies shown in Fig. 5. To create animals used in Fig. 5, a hemizygous inducible Cre driver line (driven by a CAG promoter) that our group has previously validated (JAX stock no. 004682) (29, 32, 33) was crossed to a double mutant *Syngap1*$^{+/lx}$/Thy1-GCaMP6s4.3 line. Only triple mutant animals were selected for experiments. Animals expressing the inducible Cre transgene were injected (intraperitoneal) with TMX for 5 d starting at PND 60. TMX (Sigma T5648) was prepared by dissolving it into absolute ethanol (Acros/Fisher Scientific 61510-0010) (10% of final volume) by sonication to which corn oil was added for a final dosage of 100 mg/kg, injectable concentration of 20 mg/mL, and volume of 5 mL/kg. For all studies, the experimenter was blind to genotype at the time of data acquisition and analysis.

Slice Electrophysiology.

Preparation of barrel cortex slices. Thalamocortical slices (350 μm) containing the barrel cortex were prepared as described previously (42). P21 to P30 mice of either sex were decapitated under isofluorane in accordance with Scripps regulation. The brain was rapidly removed in ice-cold artificial cerebrospinal fluid (aCSF) containing the following (in mM): 119 NaCl, 2.5 KCl, 1.3 $MgSO_4$, 2.5 CaCl2, 1 NaH_2PO_4, 11 D-glucose, and 26.3 NaHCO3, pH 7.4, 300 to 310 mOsm bubbled with 95% CO_2 and 5% O_2. Slices were cut on a vibrating microtome (Candem Instruments), transferred to a submersion chamber (Warner Instruments) at 32 to 34 °C for 30 min, and then kept at room temperature until recording (1 to 6 h).

All recordings were made at room temperature in standard aCSF in slices containing the barrel cortex. The barrel subfield was identified by transillumination at 4× by the presence of three to five ∼300-μM wide barrels in L4. Whole-cell patch-clamp recordings of L2/3 excitatory cells were made in one of the barrel columns under visual guidance by infrared differential interference contrast microscopy at 40×. L2/3 excitatory cells were identified by their soma shape and their location ∼150 μM below the L1–L2 boundary. As expected for pyramidal neurons (43, 44), all cells showed regular spiking responses to positive current injections. Experiments were made with borosilicate patch pipettes (3 to 5 mΩ) filled with a solution containing the following (in mM): 116 K-gluconate, 6 KCl, 2 NaCl, 0.5 EGTA, 20 Hepes, 4 Mg-ATP, 0.3 Na-GTP, and 10 Na2-phosphocreatine (pH: 7.3, 280 mOsm).

Whole-cell recording of STD-LTP and LTD. The stimulating electrode was placed accurately in an L4 barrel under visual guidance in a transilluminated slice.

EPSPs were evoked via a concentric bipolar stimulating electrode placed within the base of a barrel in L4, vertically aligned to the site of the recording. EPSPs were evoked at a constant rate of 0.1 Hz. Timing-based plasticity was induced as previously described (45). Briefly, after a stable baseline period of 10 min, single EPSPs were paired with single APs evoked by the minimum current injection required to evoke an AP at precise delay before or after each AP. To induce STD-LTP, the postsynaptic AP was evoked within 10 ms after the onset of the EPSP, whereas STP-LTD was induced by evoking the postsynaptic AP 20 ms before the onset of the EPSP. After 75 pairing sweeps, current injection was suspended and EPSP slope was monitored for 30 min. Presynaptic stimulation intensity remained constant throughout the experiment. Series resistance was compensated. Input resistance was monitored, and cells were discarded if the resting membrane potential changed by more than 8 mV. For quantification of LTP and LTD, the ratio of postpairing slope during 10 min beginning and 10 min after the end of pairing to that in the baseline was calculated. Only the initial slope (first 2 ms) of the EPSP was analyzed.

Electrophysiological data acquisition and storage. All signals were amplified using Multiclamp 700B (Molecular Devices), filtered at 4 kHz, digitized (10 kHz), and stored on a personal computer for offline analysis. Analog to digital conversion was performed using the Digidata 1440 A system (Molecular Devices). Data acquisitions and analyses were performed using pClamp 10.2 software package (Clampex and Clampfit programs; Molecular Devices).

Sensory Manipulation. For sensory deprivation experiments, we employed the SWE paradigm. All contralateral whiskers but one (usually, but not always, β whisker) were trimmed; ipsilateral whiskers were left intact. Trimming started immediately after the last baseline session by cutting whiskers to fur level using microscissors under microscope while mice were under low anesthesia (1.5 to 2% isoflurane). Whiskers were retrimmed every other day for a maximum of 21 d by lightly anesthetizing mice (1.5 to 2% isoflurane).

Chronic Cranial Window Implantation. For Thy1-GCaMP6s4.3 and Thy1-GFP mice experiments, both male and female mice at least 8 wk of age were fitted with a chronic cranial window and implanted with a titanium headpost according to established procedures with minor modifications (31). Briefly, animals were anesthetized with isoflurane (5% induction, 1.5 to 2% maintenance) and intraperitoneal injection (IP) injected with a mixture of dexamethasone (4 mg/kg), Rimadyl (carprofen 10 mg/kg), and Enroflox (enrofloxacin 5 mg/kg). Animals were mounted on a stereotaxic frame (David Kopf Instruments), and body temperature was maintained with a thermal regulator (Harvard Apparatus). The scalp was shaved and sterilized with alternating swabs of Betadine and 70% alcohol. A small skin flap was removed, the periosteum was gently cleared, and the skull was scraped with a scalpel. A small circular craniotomy was made over the left barrel cortex (3-mm diameter; center relative to bregma: lateral 3.5 mm; posterior 1.8 mm) using a dental drill, and the dura was left intact. Two 3-mm glass coverslips were glued onto a 5-mm glass coverslip, and the cranial window was sealed by gluing these coverslips directly to the bone (VetBond, 3 M). The titanium headpost was implanted by adhering it directly to the bone using VetBond and then dental cement (Metabond, Parkell). Animals recovered on a warm blanket before being placed back in their home cage. Rimadyl and Enroflox was injected (5 mg/kg) for 3 consecutive days after surgery for pain management. Animals were left to recover at least 10 d before subsequent experiments.

IOS Imaging. Animals of at least 8 wk of age were IP injected with the sedative chlorprothixene (1 μg/g) and were anesthetized with a lower dose of isoflurane (5% induction, 0.5% maintenance) (46). Imaging was performed under a 4× objective on an upright microscope frame (BW51X; Olympus). The barrel cortex was illuminated with 630-nm light emitting diodes (LED) mounted on the 4× objective. The images were acquired with a Zeiss Axiocam camera (Carl Zeiss Microscopy Inc.) controlled by μManager software (Open Imaging, Inc.). Acquisition rate was ∼10 Hz. Whiskers were deflected using a piezoelectric bending actuator controlled by a linear voltage amplifier (Piezo Systems Inc.). A single sinusoidal wave with a 5-ms rise and a 5-ms decay time was generated using Clampex software (Molecular Devices). Bending of the piezo was calibrated using a laser-based displacement device (LD1610-0.5 Micro-Epsilon). A single whisker deflection was ∼200 μm at 2 mm away from the whisker pad.

Analysis of IOS imaging. Each IOS imaging trial consisted of a 2-s baseline imaging period followed by 40 deflections at 10 Hz. We performed 50 to 70 trials for each whisker and averaged them using Intrinsic Optical (IO) and Voltage Sensitive Dye (VSD) Signal Processor plugin in ImageJ (47). Images taken between 1 s and 3 s after the start of the stimulus were averaged and defined as the response. IOS images were obtained by calculating the (response – baseline)/baseline value for each pixel using custom scripts written in Matlab (MathWorks), according to established procedures (48, 49). Investigator was blind to animal genotype at the time of the analyses. Briefly, images were first filtered with a Gaussian filter. Afterward, a baseline and a response region were manually selected in the final IOS image to minimize contamination by blood vessels (48). Response size was determined as the minimum value of the response region subtracted from the median of the baseline region. Image thresholding was performed in the response region to determine the area of activation. Relative thresholding values were set at 50% of the response size for each image.

In Vivo Two-Photon Imaging. In vivo two-photon imaging was performed in L2/3 of the barrel cortex. For each imaging session, mice of at least 8 wk of age were anesthetized with isoflurane (5% induction, 1.5 to 2% maintenance). Individual sessions lasted 40 to 90 min, after which animals were returned to their home cage (one animal per cage). Following recovery from surgery, IOS imaging was performed through the cranial window, as described above, using light (0.5 to 1%) isoflurane anesthesia to locate PW areas (typically β and C2 whisker). Imaging was performed with a VivoScope two-photon microscope equipped with a resonant scanner (Scientifica). The light source was a Mai Tai HP 100 femtosecond-pulse laser (Spectra-Physics) running at 940 nm for GCaMP and 910 nm for GFP. The objective was a 16× water immersion lens with 0.8 numerical aperture (NA) (Nikon) for GCaMP imaging and ULTRA 25× with 1.05 NA (Olympus) for GFP imaging. Images were acquired using ScanImage 5 (https://vidriotechnologies.com). For GCaMP6 imaging, images (512 × 512 pixels, 4× zoom, 150 × 150 μm) of L2/3 cells (70 to 250 μm below the pia) were collected at 10 Hz. For GFP imaging of L2/3 axonal boutons from one wS1 cortical area (usually, but not always, β), image stacks were collected 100 to 200 μm below the pia at 1-μm intervals. Each z-image was 1,024 × 1,024 pixels, 4× zoom, and was integrated over 10 to 20 s at each depth. Laser power at the sample was estimated to be <80 mW for GCaMP6 experiments and <30 mW for eGFP experiments. A similar number of imaging depths and same number of imaging sessions at similar depths were acquired for each animal. The head of the animals was in a fixed position across sessions to ensure consistent orientation of imaging planes. For repeated imaging, areas were reacquired using blood vessels as landmarks.

Analysis of axon bouton dynamics in the barrel cortex. The exact same axon shafts residing in a specific wS1 area (usually, but not always, β receptive area) were imaged throughout four imaging sessions (i.e., two baseline and two plasticity sessions). Relative to whisker trimming day (i.e., day 0), the first baseline was always collected at day −11 and the second baseline always at day 0, right before whisker trimming (all contralateral whiskers but β, typically). Plasticity sessions were always completed at day 3 and day 14 relative to trimming day. Axonal segments (20 to 125 μm) visible in L2/3 of the β receptive area were identified from the image stacks from their location and morphology. In total, 3 to 11 axonal segments per animal were collected and considered for analysis if visible throughout the four imaging sessions. Within animals, axon bouton dynamics were compared between baseline and plasticity sessions (11-d time window in both types of sessions). For calculation of bouton TOR and formation and elimination rates, z-stack images containing the axon segment of interest were sum intensity projected to include the whole arbor. Next, the axon of interest was traced manually with a line selection tool in ImageJ (NIH). The intensity along the selected line was measured. Boutons that exhibited a peak intensity >1.5 times the average axon shaft intensity on session one were selected for analysis. A bouton was scored as stable if this bouton maintained its peak intensity >1.5 times than the axon shaft. New peaks of intensity >1.5 times the average axon segment intensity were scored as gain. If the peak of intensity of a bouton dropped below 1.2 times the average axon segment intensity, it was scored as a loss. In the case of finding intensity peaks in close proximity to each other, intensity peaks were scored as distinct boutons if they were at least 2 μm apart. TOR was calculated as TOR (t_1, t_2) = (N_{gained} + N_{lost})/(2 × N(t_1)) (28, 50). The percentage of boutons formed or eliminated is defined as the number of boutons formed or eliminated divided by the number of existing boutons at the first session compared. The change in TOR, change in formation, and change in elimination refers to the percentage of increment measured over a given interval (51).

Analysis of GCaMP activity in the barrel cortex. Neuronal populations residing in two different wS1 areas (usually populations from β and C2 receptive fields) were studied during four different imaging sessions (i.e., two baseline sessions and two plasticity sessions). For Thy1-GCaMP6s4.3/*Syngap1* mice, the first baseline session was performed at day ∼ −13 (−13.10 ± 2.68) and the second baseline always at day 0 right before trimming (relative to whisker trimming day; i.e., day 0). The first plasticity sessions were completed at day ∼12 (12.10 ± 0.10) and second plasticity sessions at day ∼20 (19.52 ± 0.98) relative to trimming day. For experiments performed with Thy1-GCaMP6s4.3/Cre-ER/*Syngap1*$^{+/lx\text{-}st}$, the first baseline sessions were performed at day ∼ −9 (−8.63 ± 0.34) and the second baseline always at day 0 right before trimming.

After whisker trimming, sessions were always completed at day 12 and day 21 for the first and second plasticity sessions, respectively.

Within each imaging area, all neurons that could be visualized in each of the four sessions were studied, irrespective of levels of activity or responsiveness to the deflection of the PW and NPW. PW and NPW deflection responses were analyzed for each neuron visualized in both imaging areas. For each imaging session, extraction of ΔF/F of calcium images was performed in Matlab R2015b using the FluoroSNNAP15.04.08 plugin (52). Regions of interest (ROIs) corresponding to identifiable cell bodies along the four imaging sessions were selected manually. The fluorescence time course was measured by averaging all pixels within the ROI, then corrected for neuropil contamination. The neuropil ROIs were also manually drawn where there were no visible cell bodies and were the same for all cells within an imaging frame. After neuropil correction, the ΔF/F of each ROI was calculated as (F − F0)/F0, where F0 was the mean of the lower 50% of the proceeding 10-s period. For the first 10-s period, a minimum value of F0 was used (52). A template search–based algorithm was used in order to detect calcium events using built-in templates in FluoroSNNAP15.04.08. Whisker-stimulation–induced activity was recoded over a 2-min period from the same ROIs (PW and NPW stimulation activity was recorded for each ROI). Whisker stimulation consisted of 10 whisker stimulations at 20 Hz with an intertrain interval of 5.12 s. For each type of whisker deflection (i.e., PW or NPW), a total of 21 trains were given during a 2-min period, from which the greatest ΔF/F value per cell per type of whisker deflection (PW or NPW) was taken for analysis. We used custom-written R scripts for the extraction and processing of the maximum ΔF/F amplitude induced by PW and NPW stimulation (1-s window/stim) per session in each cell. Based on their maximum ΔF/F response to the PW stimulations during baseline sessions, cells were classified into low-, mid-, and high-active cells as previously described (8). Briefly, low-active cells comprised 63.3% of the total population included for analyses. Mid active and high active represent 29.6% and 7.1% of the total population, respectively. Next, the maximum ΔF/F response per cell was averaged per type of session (i.e., baseline or plasticity), and the change in the averaged ΔF/F (i.e., ratio of plasticity/baseline) of each cell was used to study the effect of whisker trimming on neuronal dynamics.

Statistics. *SI Appendix*, Table S1 contains all statistical comparisons, including those that were not significant and therefore not explicitly mentioned in the results or figure legends. Data analyses were conducted in Matlab (MathWorks, version 2013b and 2015b), R studio (RStudio, Inc.), and GraphPad Prism 8 (GraphPad Software). D'Agostino–Pearson omnibus normality tests were applied to determine data distributions, and the appropriate parametric or nonparametric statistical test was performed accordingly. For analysis of electrophysiological data, one-sample *t* test, two-sided Student's *t* test, and two-way ANOVA (mixed model) was used. For analysis of axon boutons imaging data, the following tests were used: two-sided paired Student's *t* test was used for within-genotype comparisons of TOR, formation, and elimination before and after sensory deprivation. For within-genotype comparisons of change in TOR, change in formation, and change in elimination, one-sample *t* test and Wilcoxon signed-rank tests were used. For genotype comparisons of change in TOR, change in formation and change in elimination Mann–Whitney *U* tests were used. For within-genotype comparisons of GCaMP imaging data, one-sample *t* test and Wilcoxon signed-rank tests were used. For genotype comparisons of GCaMP imaging data, two-sided Student's *t* test or Mann–Whitney *U* test were used. Data throughout the text are presented as mean ± SEM and median. Differences were considered to be significant for $P < 0.05$.

Data Availability. All data that support the findings of this study are available from the corresponding author upon reasonable request by email.

ACKNOWLEDGMENTS. This work was supported in part by NIH grants from the National Institute of Mental Health (MH096847 and MH108408) and the National Institute for Neurological Disorders and Stroke (NS064079 and NS110307). N.L. was supported by a generous postdoctoral training fellowship from the SynGAP Research Fund.

1. D. H. Ebert, M. E. Greenberg, Activity-dependent neuronal signalling and autism spectrum disorder. *Nature* **493**, 327–337 (2013).
2. T. Bourgeron, From the genetic architecture to synaptic plasticity in autism spectrum disorder. *Nat. Rev. Neurosci.* **16**, 551–563 (2015).
3. L. de la Torre-Ubieta, H. Won, J. L. Stein, D. H. Geschwind, Advancing the understanding of autism disease mechanisms through genetics. *Nat. Med.* **22**, 345–361 (2016).
4. V. Anggono, R. L. Huganir, Regulation of AMPA receptor trafficking and synaptic plasticity. *Curr. Opin. Neurobiol.* **22**, 461–469 (2012).
5. E. R. Kandel, Y. Dudai, M. R. Mayford, The molecular and systems biology of memory. *Cell* **157**, 163–186 (2014).
6. G. Buzsáki, Neural syntax: Cell assemblies, synapsembles, and readers. *Neuron* **68**, 362–385 (2010).
7. D. J. Margolis, H. Lütcke, F. Helmchen, Microcircuit dynamics of map plasticity in barrel cortex. *Curr. Opin. Neurobiol.* **24**, 76–81 (2014).
8. D. J. Margolis *et al*., Reorganization of cortical population activity imaged throughout long-term sensory deprivation. *Nat. Neurosci.* **15**, 1539–1546 (2012).
9. L. Cohen *et al*., Time-lapse electrical recordings of single neurons from the mouse neocortex. *Proc. Natl. Acad. Sci. U.S.A.* **110**, 5665–5670 (2013).
10. D. E. Feldman, M. Brecht, Map plasticity in somatosensory cortex. *Science* **310**, 810–815 (2005).
11. A. Maffei, K. Nataraj, S. B. Nelson, G. G. Turrigiano, Potentiation of cortical inhibition by visual deprivation. *Nature* **443**, 81–84 (2006).
12. M. A. Gainey, D. E. Feldman, Multiple shared mechanisms for homeostatic plasticity in rodent somatosensory and visual cortex. *Philos. Trans. R. Soc. Lond. B Biol. Sci.* **372**, 20160157 (2017).
13. T. C. Griffen, A. Maffei, GABAergic synapses: Their plasticity and role in sensory cortex. *Front. Cell. Neurosci.* **8**, 91 (2014).
14. N. S. Desai, L. C. Rutherford, G. G. Turrigiano, Plasticity in the intrinsic excitability of cortical pyramidal neurons. *Nat. Neurosci.* **2**, 515–520 (1999).
15. M. E. Lambo, G. G. Turrigiano, Synaptic and intrinsic homeostatic mechanisms cooperate to increase L2/3 pyramidal neuron excitability during a late phase of critical period plasticity. *J. Neurosci.* **33**, 8810–8819 (2013).
16. F. K. Satterstrom *et al*.; Autism Sequencing Consortium; iPSYCH-Broad Consortium, Large-scale exome sequencing study implicates both developmental and functional changes in the neurobiology of autism. *Cell* **180**, 568–584.e23 (2020).
17. M. Kilinc *et al*., Species-conserved SYNGAP1 phenotypes associated with neurodevelopmental disorders. *Mol. Cell. Neurosci.* **91**, 140–150 (2018).
18. G. Rumbaugh, J. P. Adams, J. H. Kim, R. L. Huganir, SynGAP regulates synaptic strength and mitogen-activated protein kinases in cultured neurons. *Proc. Natl. Acad. Sci. U.S.A.* **103**, 4344–4351 (2006).
19. L. E. Vazquez, H. J. Chen, I. Sokolova, I. Knuesel, M. B. Kennedy, SynGAP regulates spine formation. *J. Neurosci.* **24**, 8862–8872 (2004).
20. T. R. Gamache, Y. Araki, R. L. Huganir, Twenty years of SynGAP research: From synapses to cognition. *J. Neurosci.* **40**, 1596–1605 (2020).
21. J. H. Kim, H. K. Lee, K. Takamiya, R. L. Huganir, The role of synaptic GTPase-activating protein in neuronal development and synaptic plasticity. *J. Neurosci.* **23**, 1119–1124 (2003).
22. E. D. Ozkan *et al*., Reduced cognition in Syngap1 mutants is caused by isolated damage within developing forebrain excitatory neurons. *Neuron* **82**, 1317–1333 (2014).
23. J. P. Clement, E. D. Ozkan, M. Aceti, C. A. Miller, G. Rumbaugh, SYNGAP1 links the maturation rate of excitatory synapses to the duration of critical-period synaptic plasticity. *J. Neurosci.* **33**, 10447–10452 (2013).
24. N. H. Komiyama *et al*., SynGAP regulates ERK/MAPK signaling, synaptic plasticity, and learning in the complex with postsynaptic density 95 and NMDA receptor. *J. Neurosci.* **22**, 9721–9732 (2002).
25. F. Gambino, A. Holtmaat, Spike-timing-dependent potentiation of sensory surround in the somatosensory cortex is facilitated by deprivation-mediated disinhibition. *Neuron* **75**, 490–502 (2012).
26. G. Feng *et al*., Imaging neuronal subsets in transgenic mice expressing multiple spectral variants of GFP. *Neuron* **28**, 41–51 (2000).
27. Q. Qiao *et al*., Long-term stability of axonal boutons in the mouse barrel cortex. *Dev. Neurobiol.* **76**, 252–261 (2016).
28. V. De Paola *et al*., Cell type-specific structural plasticity of axonal branches and boutons in the adult neocortex. *Neuron* **49**, 861–875 (2006).
29. J. P. Clement *et al*., Pathogenic SYNGAP1 mutations impair cognitive development by disrupting maturation of dendritic spine synapses. *Cell* **151**, 709–723 (2012).
30. H. Dana *et al*., Thy1-GCaMP6 transgenic mice for neuronal population imaging in vivo. *PLoS One* **9**, e108697 (2014).
31. S. D. Michaelson *et al*., SYNGAP1 heterozygosity disrupts sensory processing by reducing touch-related activity within somatosensory cortex circuits. *Nat. Neurosci.* **21**, 1–13 (2018).
32. M. Aceti *et al*., Syngap1 haploinsufficiency damages a postnatal critical period of pyramidal cell structural maturation linked to cortical circuit assembly. *Biol. Psychiatry* **77**, 805–815 (2015).
33. T. K. Creson *et al*., Re-expression of SynGAP protein in adulthood improves translatable measures of brain function and behavior. *eLife* **8**, e46752 (2019).
34. D. E. Feldman, Synaptic mechanisms for plasticity in neocortex. *Annu. Rev. Neurosci.* **32**, 33–55 (2009).
35. M. H. Berryer *et al*., Decrease of SYNGAP1 in GABAergic cells impairs inhibitory synapse connectivity, synaptic inhibition and cognitive function. *Nat. Commun.* **7**, 13340 (2016).
36. L. L. Colgin, Rhythms of the hippocampal network. *Nat. Rev. Neurosci.* **17**, 239–249 (2016).
37. C. C. Smith, L. L. McMahon, Estrogen-induced increase in the magnitude of long-term potentiation occurs only when the ratio of NMDA transmission to AMPA transmission is increased. *J. Neurosci.* **25**, 7780–7791 (2005).
38. N. J. Sofroniew, K. Svoboda, Whisking. *Curr. Biol.* **25**, R137–R140 (2015).
39. D. Feldmeyer *et al*., Barrel cortex function.*Prog. Neurobiol.* **103**, 3–27 (2013).
40. C. C. Petersen, S. Crochet, Synaptic computation and sensory processing in neocortical layer 2/3. *Neuron* **78**, 28–48 (2013).

41. National Research Council, *Guide for the Care and Use of Laboratory Animals* (National Academies Press, Washington, DC, ed. 8, 2011).
42. A. Agmon, B. W. Connors, Thalamocortical responses of mouse somatosensory (barrel) cortex in vitro. *Neuroscience* **41**, 365–379 (1991).
43. B. W. Connors, M. J. Gutnick, Intrinsic firing patterns of diverse neocortical neurons. *Trends Neurosci.* **13**, 99–104 (1990).
44. A. Agmon, B. W. Connors, Correlation between intrinsic firing patterns and thalamocortical synaptic responses of neurons in mouse barrel cortex. *J. Neurosci.* **12**, 319–329 (1992).
45. D. E. Feldman, Timing-based LTP and LTD at vertical inputs to layer II/III pyramidal cells in rat barrel cortex. *Neuron* **27**, 45–56 (2000).
46. A. L. Juavinett, I. Nauhaus, M. E. Garrett, J. Zhuang, E. M. Callaway, Automated identification of mouse visual areas with intrinsic signal imaging. *Nat. Protoc.* **12**, 32–43 (2017).
47. T. C. Harrison, A. Sigler, T. H. Murphy, Simple and cost-effective hardware and software for functional brain mapping using intrinsic optical signal imaging. *J. Neurosci. Methods* **182**, 211–218 (2009).
48. C. H. Chen-Bee, R. D. Frostig, Variability and interhemispheric asymmetry of single-whisker functional representations in rat barrel cortex. *J. Neurophysiol.* **76**, 884–894 (1996).
49. C. H. Chen-Bee *et al*., Visualizing and quantifying evoked cortical activity assessed with intrinsic signal imaging. *J. Neurosci. Methods* **97**, 157–173 (2000).
50. F. W. Grillo *et al*., Increased axonal bouton dynamics in the aging mouse cortex. *Proc. Natl. Acad. Sci. U.S.A.* **110**, E1514–E1523 (2013).
51. F. Pan, G. M. Aldridge, W. T. Greenough, W. B. Gan, Dendritic spine instability and insensitivity to modulation by sensory experience in a mouse model of fragile X syndrome. *Proc. Natl. Acad. Sci. U.S.A.* **107**, 17768–17773 (2010).
52. T. P. Patel, K. Man, B. L. Firestein, D. F. Meaney, Automated quantification of neuronal networks and single-cell calcium dynamics using calcium imaging. *J. Neurosci. Methods* **243**, 26–38 (2015).